TOPOLOGICALLY PROTECTED REFRACTION OF ROBUST KINK MODE FROM PHOTONIC CRYSTAL INTO FREE SPACE

A Dissertation

Presented to the Faculty of the Graduate School

of Cornell University

in Partial Fulfillment of the Requirements for the Degree of

Master of Science

by

Yandong Li

May 2018

ABSTRACT

Similar to those electronic topological insulators that are based on the quantum valley Hall effect [13, 35, 14], valley photonic topological insulators (PTIs) guide unidirectional electromagnetic modes. [22, 21, 5] A recent research[9] studies how that unidirectional mode couples into the free space, aiming to incorporate this PTI into integrated photonic structures. Here we focus on light-refraction from a two-dimensional valley PTI into the free space. We understand this PTI as a waveguide, model its refraction as the radiation of an array of dipoles, and demonstrate several ways to engineer its dispersion relation. We also confirm the nontrivial topology of this PTI by unveiling its non-zero Berry curvature at the valley. This study may benefit future research on photonic topological behaviors and realizing novel photonic phenomenon.

BIOGRAPHICAL SKETCH

I grew up in Nanjing (also known as Nanking), a historic city in the East China region. After I finished my high school education in Nanjing Foreign Language School, I came to the U.S. I studied engineering physics in Case Western Reserve University. In August 2016, I entered Cornell University to pursue a M.Sc. in applied physics.

This study is dedicated to my parents.

ACKNOWLEDGEMENTS

I would first like to thank Prof. Gennady Shvets for his guidance. He gives us the freedom to explore the numerous fascinating phenomenon arising from topological physics. Our group frequently brainstorm together. This contributes significantly to my and other group members' progress in physics research.

I am quite lucky to work with the brilliant people, and, more importantly, all of them are very interested in and enthusiastic about physics research. Among them Ran Gladstone, Yang Yu and Minwoo Jung work on topological photonics with me and are of my close friends. We usually discuss physics through email at late nights and during weekends. Without them, I would have proceeded much slower.

Most importantly, I would like to thank my parents. Without their support and encouragement, I could not fulfill my curiosity and proceed the study of physics.

TABLE OF CONTENTS

LIST OF FIGURES

CHAPTER 1

INTRODUCTION

The development of science is usually driven by a fusion of technological demands and fundamental discoveries. The "photonic topological insulator", as a perfect example, is the result of the evolution of photonic crystals and the exploration of topological phases.

Over the past twenty years, molding the light flow by using 2D and 3D photonic crystals has been a thriving research topic.[12] Photonic crystals can have band gaps that significantly affect the motion of photons travelling inside, which lead to promising applications in optical communications and signal processing. As researchers further investigate the "conventional" optical degrees of freedom, such as frequency, phase, polarization, etc., the topological behavior of the photonic bands start receiving more attention.[19, 5]

The physical concept of topology is tightly linked with mathematical studies of the fibre bundle.[23] In the field of solid state physics, topology has been accumulating phenomenal interest since Michael Berry discovered the Berry phase in 1984.[4] Many unique properties are associated with the Berry phase and the Berry curvature.[34] Especially, the unidirectional quantum Hall edge state is connected with the Berry curvature of the band structure.[16] In 2005, S. Raghu demonstrated a theoretical study on a photonic analogue to the quantum Hall effect, and proved the possiblity to create unidirection photonic state out of topology.[26]

For the past decade, researchers realized different photonic crystals that emulate the quantum Hall effect[32, 33, 22], quantum spin Hall effect[10, 6, 15, 22],

quantum valley Hall effect[22, 21] and quantum anomalous Hall effect[29]. The theoretically-predicted unidirectional photonic states were experimentally confirmed.[33, 29, 20, 9] Their immunity to back-reflections heralds that the topological photonic waveguides have enormous advantages over conventional waveguides.

In this study, we focus on the unidirectional chiral kink states in a photonic topological insulator (PTI) that emulates the quantum valley Hall effect.[21] Particularly, we study how such kink states refract to the free space. We model the refraction phenomenon with the radiation of an array of electric dipoles. Furthermore, we explore several ways to engineer the refraction direction by manipulating the photonic band diagram. Understanding the refraction pattern may benefit future research that pushes the valley PTI towards applications, for example, the search for practical methods to excite such kink states out of the PTI.

CHAPTER 2

THEORY

2.1 Rewritting Maxwell's Equations

Photonic crystals are made up of periodic structures, realizing a system with a spatially, periodically changing dielectric function. [26] (Fig. 2.1) This spatically periodic nature of the structure motivates us to borrow the physics of the electronic Bloch states.

$$\Phi(\mathbf{x}) = u(\mathbf{x})e^{i\mathbf{k}\cdot\mathbf{x}} \tag{2.1}$$

The Bloch state is a product of a plane wave $e^{i\mathbf{k}\cdot\mathbf{x}}$ and a periodic function $u(\mathbf{x})$, where $u(\mathbf{x})$ has the same periodicity as the crystalline lattice.

To draw parallels between electronic states and electromagnetic states, the first step is to write Maxwell's equations in the form of the Schrödinger Equation[8].

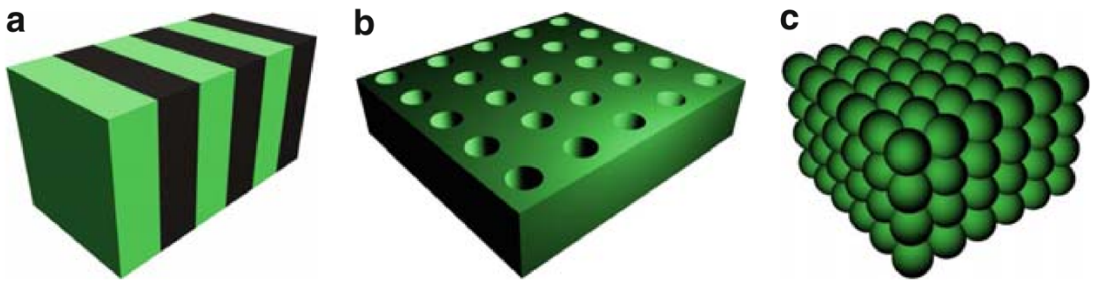

Figure 2.1: 1D, 2D and 3D photonic crystals[28]

$$\mathbf{M} = \begin{bmatrix} \varepsilon_0\bar{\varepsilon} & \frac{1}{c}\bar{\xi} \\ \frac{1}{c}\bar{\zeta} & \mu_0\bar{\mu} \end{bmatrix} \quad \mathbf{N} = \begin{bmatrix} 0 & i\nabla\times\mathbf{I_3} \\ -i\nabla\times\mathbf{I_3} & 0 \end{bmatrix} \tag{2.2}$$

$$\mathbf{f} = \begin{bmatrix} \mathbf{E} \\ \mathbf{H} \end{bmatrix} \quad i\frac{\partial \mathbf{f}}{\partial t} = \mathbf{H}\mathbf{f} \tag{2.3}$$

In this form[27, 26], $\mathbf{f} = [\mathbf{E}, \mathbf{H}]^T$ represents a classical electromagnetic wave. $\mathbf{E}$ and $\mathbf{H}$ represent the electric and magnetic fields. The effective Hamiltonian $\mathbf{H} = \mathbf{M}^{-1}\cdot\mathbf{N}$. Matrix $\mathbf{M}$ describes the material, with the real-valued parameters $\bar{\varepsilon}, \bar{\mu}, \bar{\xi}, \bar{\zeta}$ representing the permittivity, the permeability and the two magneto-electric coupling tensors. $\mathbf{I_3}$ is a 3-by-3 identity matrix. With this re-formalism of Maxwell's equations, S. Raghu and F. D. M. Haldane explained the Bloch's theorem, the geometric phase, the Chern number, etc. from the perspective of photonics.[26]

2.2 the Chern Number

Although the geometric phase was discovered first in optics by S. Pancharatnam[24], photonic geometric phase caught attention after the discovery of Berry phase[4] in an electronic system. Therefore, we start to introduce the topology by discussing the electronic system.

For a Bloch wave function $|u(\mathbf{k})\rangle$, when $\mathbf{k}$ is varied along a path $\mathbf{C}$, $|u(\mathbf{k})\rangle$ accumulates a phase $\gamma = \int_{\mathbf{C}} d\mathbf{k}\cdot\mathscr{A}(\mathbf{k})$.

$\mathscr{A}(\mathbf{k})$ is called the Berry connection, similar to the vector potential. $\mathscr{A}(\mathbf{k})$ is defined as,

$$\mathscr{A}(\mathbf{k}) = i \langle u(\mathbf{k}) | \nabla_{\mathbf{k}} | u(\mathbf{k}) \rangle \tag{2.4}$$

For the same Hamiltonian, both $|u(\mathbf{k})\rangle$ and $e^{i\phi(\mathbf{k})}|u(\mathbf{k})\rangle$ are indistinguishable solutions. Under the gauge transformation $|u(\mathbf{k})\rangle \rightarrow e^{i\phi(\mathbf{k})}|u(\mathbf{k})\rangle$, the Berry curvature experiences $\mathscr{A}(\mathbf{k}) \rightarrow \mathscr{A}(\mathbf{k}) - \nabla_{\mathbf{k}}\phi(\mathbf{k})$. Therefore the Berry connection is gauge-dependent.[34] Hence, in general, the phase γ is gauge-dependent. However, for a closed path $\mathbf{C}$, γ can only change by a integer multiple of 2π under gauge transformations.[4] Therefore, for any closed path $\mathbf{C}$, γ becomes a gauge-invariant quantity, and is known as the Berry phase. γ is defined as,

$$\gamma = \oint_{\mathbf{C}} d\mathbf{k} \cdot \mathscr{A}(\mathbf{k}) \tag{2.5}$$

According to Stokes' theorem, we can rewrite the Berry phase as a surface integral,

$$\gamma = \iint_{\mathbf{S}} d\mathbf{S} \cdot \Omega(\mathbf{k}) \tag{2.6}$$

where

$$\Omega(\mathbf{k}) = \nabla_{\mathbf{k}} \times \mathscr{A}(\mathbf{k}) \tag{2.7}$$

By integrating the Berry curvature over a closed manifold, one should always get a integer multiples of 2π.[34] (For example, a parallelogram in 2D with periodic boundary conditions on both of the two pairs of parallel sides is equivalent to a torus manifold.)

$$\iint_S \Omega(\mathbf{k})\, ds = \mathcal{N} \cdot 2\pi \tag{2.8}$$

That integer is the Chern number.

For a material with a complete band gap, if the Fermi level is inside that band gap, the material functions as an insulator. A "gap Chern number" associated with that complete band gap is defined as the sum of the Chern numbers of all the bands below the gap.[19, 29] Therefore, we can classify different (insulator-like) materials according to their gap Chern numbers.

It may be worthy to mention that, although people usually consider a **k**-dependent geometric phase, the same mathematics and physics apply to a geometric phase depending on another parameter. We consider a **k**-dependent geometric phase because the Hamiltonian of the system in this study depends on **k**.

2.3 Bulk-Edge Correspondence

An interesting phenomenon emerges when we join two different materials with different Chern numbers together. For example, let us consider a heterostructure of two bulk crystalline materials and one boundary. (figure 2.2) Along that boundary, one or more edge modes exists. Meanwhile, in the momentum-space, the frequency dispersion relation of this structure has a band gap. And, in that band gap, there are the dispersion relations of the edge modes.

It is the difference between the gap Chern numbers of the two materials that determines the behavior and the number of the edge modes. When material A

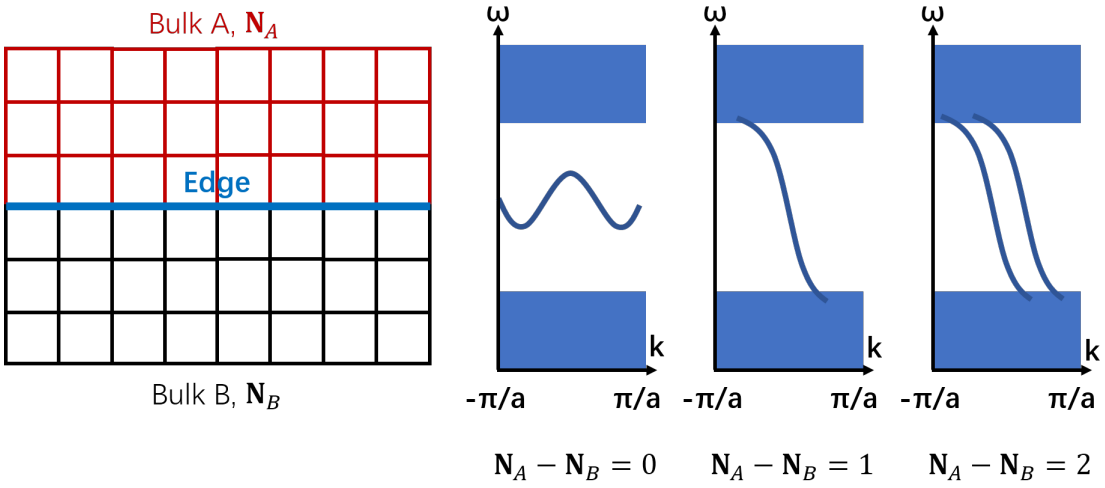

Figure 2.2: The Bulk-Edge correspondence

and material B have identical Chern numbers, the frequency spectrum of the edge mode does not span the entire band gap. Conversely, when A and B have different gap Chern numbers, the edge modes' frequency spectra always cover the entire band gap, and, the number of such edge modes equals to that Chern-number-difference.

$$N_{UEM} = | \mathcal{N}_A - \mathcal{N}_B | \tag{2.9}$$

where N_{UEM} represents the number of Unidirectional Edge Modes.

The edge mode that occurs in the later case has another interesting property, unidirectionality. Since the frequency spectra of the edge modes monotonically spans the entire band gap, their slopes do not change sign. That means their group velocities ($\propto \frac{\partial \omega}{\partial k}$) do not change directions.

2.4 Design of the PTI

Before introducing the design of the photonic topological insulator (PTI) emulating the valley Hall effect, we briefly discuss the valley magnetic moment in an electronic system, graphene. Valleys are the K and K′ points in the first Brillouin zone of graphene. The reason why valleys are interesting is that, for a electron, an intrinsic magnetic moment results from valleys. Furthermore, only in inversion-symmetry broken systems, can that valley magnetic moment be non-zero. This leads to a valley Hall effect that will be discussed below.[35]

Starting from the tight binding model[3], I conceptually demonstrate this band gap opening. The electronic wavefunction can be described as eq. 2.10, where ϕ_A is the wavefunction centered at A-typed atoms and ϕ_B is that centered at B-typed atoms. The wavefunctions are Bloch states, following the form of equation 2.1.

$$\Psi = \sum_{A} e^{i\mathbf{k}\cdot\mathbf{r_A}}\phi_A(\mathbf{r}-\mathbf{r_A}) + \lambda \sum_{\mathbf{B}} \mathbf{e}^{\mathbf{ik}\cdot\mathbf{r_B}}\phi_{\mathbf{B}}(\mathbf{r}-\mathbf{r_B}) \tag{2.10}$$

For graphene, the spatial distributions of ϕ_A and ϕ_B are the same. For the inversion-symmetry-broken graphene, the distributions are different, resulting in a difference between the two diagonal elements of the Hamiltonian. Therefore, a direct band gap occurs at the K(K′) point (Fig. 2.3 (b)); while, when inversion symmetry is conserved (figure 2.3 (a)), there is a Dirac point. The band diagrams of the unperturbed and perturbed graphene are calculated using Mathematica and presented in figure 2.3 (a,b).

Di Xiao and Qian Niu demonstrated that, for the energy bands of the

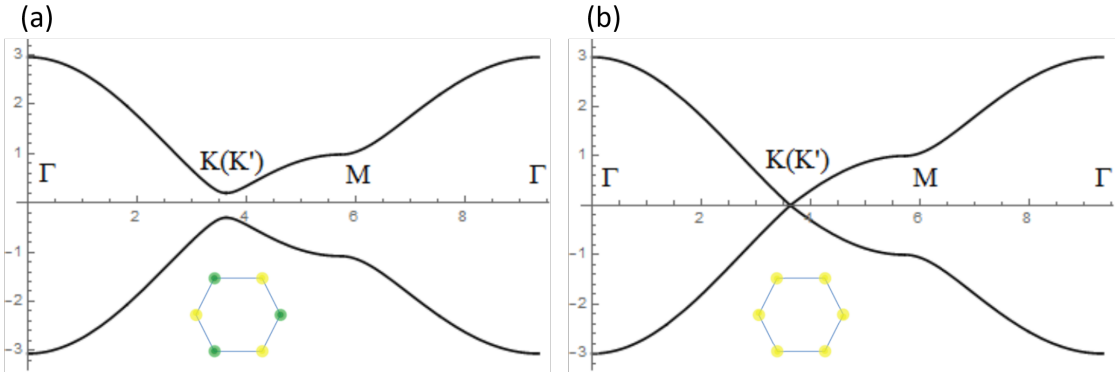

Figure 2.3: The band diagrams of graphene and inversion-symmetry-broken graphene

inversion-symmetry-broken graphene, the electron's orbital magnetic moment is concentrated in the valleys.[35] The orbital magnetic moment in the K valley has the opposite sign of that in the K' valley. Furthermore, the Berry curvature is distributed over the Brillouin zone in a very similar way, also concentrating in the valleys and having opposite signs in the two different valleys. Therefore, an integration of the Berry curvature over the entire first Brillouin zone gives a zero total Chern number. That zero total Chern number is due to the preserved time reversal symmetry.[35] However, since the Berry curvature is concentrated in the valley, the integration of the Berry curvature over one valley is non-zero. That integration is defined as the valley Chern number. Hence, at the boundary between the two different inversion-symmetry-broken graphene-like systems, the valley Chern number changes by an integer number. For example, valley Chern numbers of the AB- and BA- stacked bilayered graphene differ by ±2, indicating that two unidirectional edge modes exist at every valley.[14] This unidirectional phenomenon is directly related to inversion symmetry breaking. Therefore, we call it topologically-protected unidirectionality. Historically, edge modes that occur at the boundary between graphene-like systems are referred

to as ”kink” modes.[14] Due to the unique properties of these kink modes, we refer them as topologically-protected kink modes (TPKMs). Such TPKMs are immune to local impurities, provided there is no inter-valley scattering.

The existence of two TPKMs between AB- and BA-stacked bilayered graphene was experimentally confirmed by Long Ju. [13] Tzuhsuan Ma started to consider a photonic analog.[21] The hexagonal unit cell with a cylindrical dielectric rod at the center has a Dirac point at K(K′) points in the band structure. This phenomenon is similar to graphene, before breaking inversion symmetry. By replacing the cylindrical rods with the triangular rods, we lift the inversion-symmetry of the unit cell and open a band gap at the K(K′) point.

Joining the two oppositely-perturbed photonic crystals together, we obtain a interface separating them. Tzuhsuan Ma and Gennady Shvets demonstrate that this interface acts as a waveguide, carrying one TPKM per valley, robust to local impurities.[21] This phenomenon suggests this photonic crystal is topologically non-trivial, similar to the inversion-symmetry-broken graphene, such as the AB- and BA- stacked bilayer graphene and MoS_2.

2.5 Computation

In this study, we use COMSOL Multiphysics to perform numerical computations. COMSOL Multiphysics is a simulation software using the finite element method to solve differential equations.[1] Particularly, we use the radio frequency and wave optics modules for this study. In this study, we only consider 2D cases, for computational convenience. Also, we only study the TE polarization (i.e. electric field in the 2D plane and magnetic field perpendicular to the

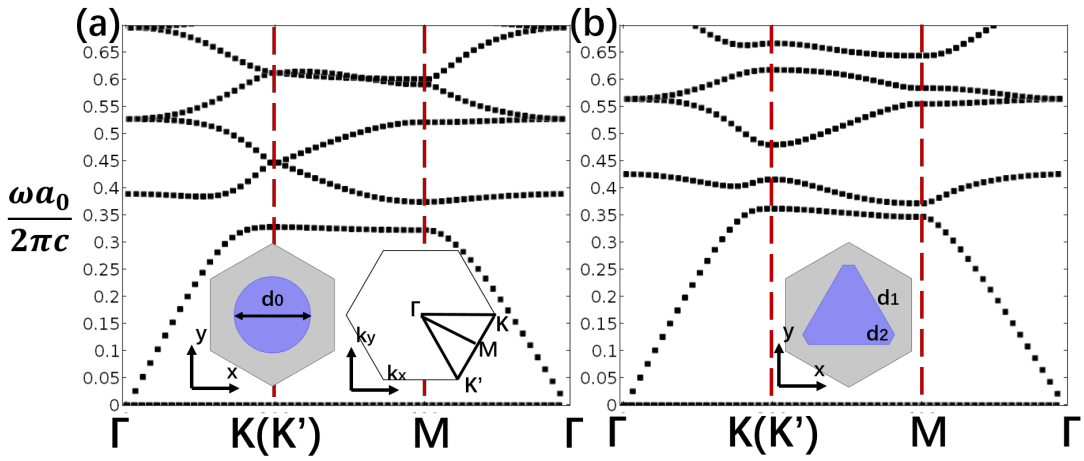

Figure 2.4: The band diagrams of photonic crystals before and after inversion-symmetry-breaking

(a) Before inversion-symmetry-breaking. A Dirac point occurs at the K(K′) point and at $\frac{\omega a_0}{2\pi c} = 0.445$. (b) After inversion-symmetry-breaking. A complete band gap opens around $\frac{\omega a_0}{2\pi c} = 0.445$. The blue region represents silicon ($\varepsilon = 13$); the grey region represents air ($\varepsilon = 1$). $d_0 = 0.615a_0$, $d_1 = 0.64a_0$, $d_2 = 0.09a_0$, where a_0 is the lattice constant.

2D plane).

2.5.1 Unit Cell, Eigen Frequency Computation

To obtain a numerical solution to the photonic band diagram, we solve for the **k**-dependent eigen-frequencies of the unit cell. We implement the phased-shifted periodic boundary conditions for all the three pairs of parallel sides of the hexagonal unit cell. The periodic boundary condition ensures that, the electromagnetic field profile at one side is a copy of that at the other. This emulates that the entire 2D space is packed with the hexagonal unit cells. Then, we alter

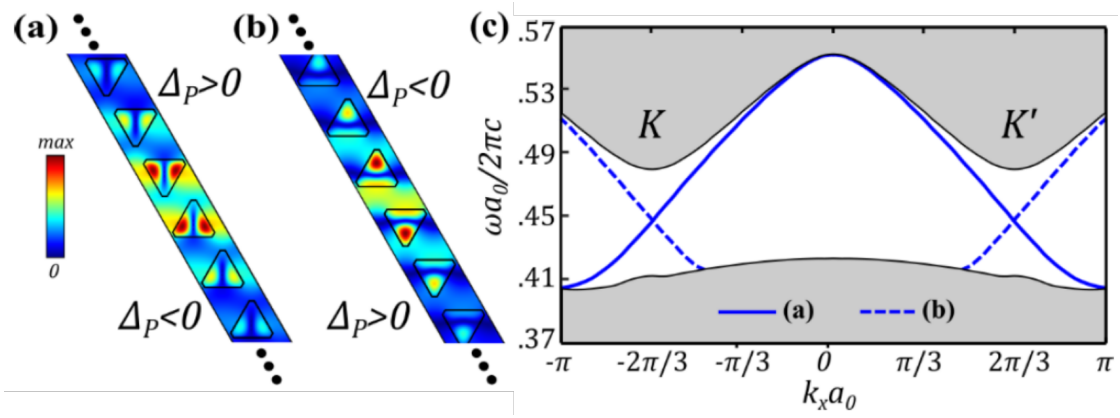

Figure 2.5: Dispersion relation of the TPKMs [21]

(a) and (b) Two types of interfaces between the two differently inversion-symmetry-broken photonic crystals. There are ten unit cells at each side of the interface. Only three of them are shown in the graph. (c) The dispersion relation of the TPKMs along the two types of interfaces. At one valley, the slope of the dispersion does not change sign.

(k_x, k_y) to sweep along the contour $\Gamma \rightarrow K(K')$, $K(K') \rightarrow M$ and $M \rightarrow \Gamma$ in the first Brillouin zone. For every set of parameters (i.e. k_x and k_y), COMSOL solves for the eigen-frequencies. After combining all the eigen-frequencies along that contour, we obtain the sphotonic band diagram. (figure 2.4)

2.5.2 Supercell, Eigen Frequency Computation

To compute the dispersion of the TPKM, we need to simulate a infinite 2D domain where positively-perturbed unit cells fill one half and negatively-perturbed unit cells fill the other. Hence, we draw one slice of the infinite 2D domain and implement periodic boundary condition on the left and right boundaries. Although this set-up is not extending infinitely upwards and downwards,

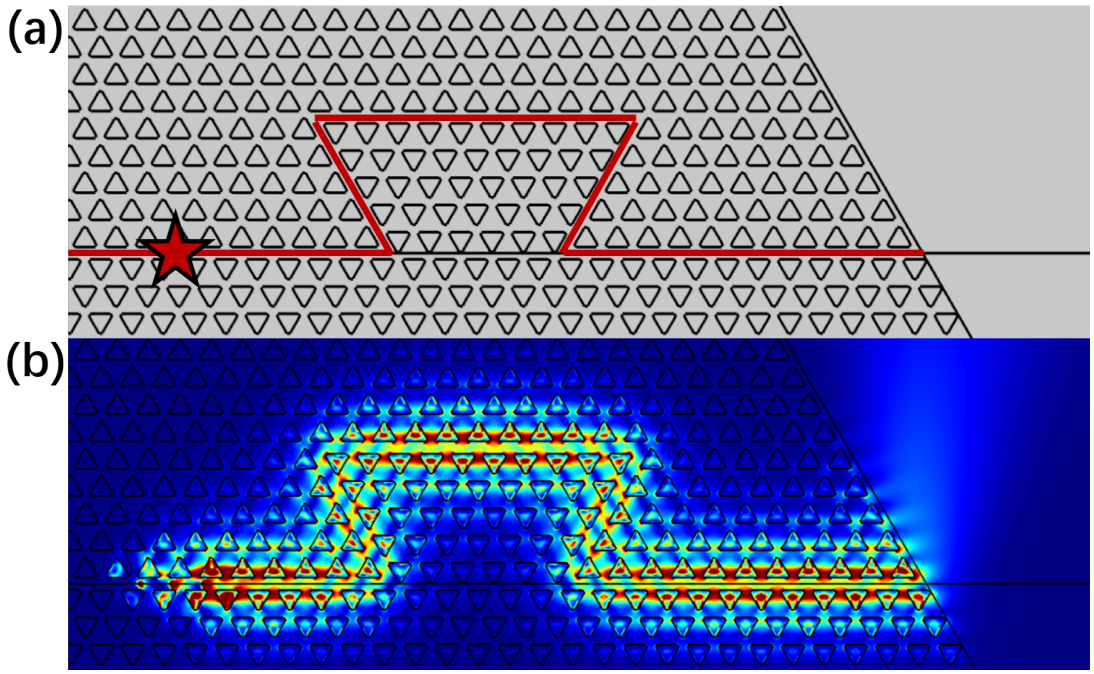

Figure 2.6: Unidirectional propagation of the TPKM

(a) The platiform in COMSOL simulation. The red line outlines the boundary between two different inversion-symmetry-broken photonic crystals. The source is at the position of the star, emitting valley-polarized beam. (b) The unidirectionality of the TPKM is immune to that Ω shape line. The color represents time averaged energy distribution.

it is still a good platiform to simulate the TPKM because the TPKM decays exponentially along the direction perpendicular to the interface. Consequently, far from the interface, the electromagnetic field intensity is negligible. Hence, simulations on this set-up should provide accurate dispersion relation of the TPKM.2.5

2.5.3 Driven Simulation

We can also introduce sources in COMSOL. For example, figure 2.6 shows a set-up of a driven simulation. The channel is the same as figure 2.5 (b). Figure 2.5 (c) shows that this channel has only two eigen modes at a frequency inside the band gap. The two eigen modes have opposite wave numbers. We aim to excite the mode with a negative group velocity (negative slope), at $k_x a_0 = -\frac{2\pi}{3}$. Therefore, as this mode propagates rightwards by a distance of a_0, the field profile should obtain a phase delay of $\frac{2\pi}{3}$. We use three electric dipoles with different phases to excite them. The right dipole leads its adjacent left dipole a phase of $\frac{4\pi}{3}$ (equivalent to a phase delay of $\frac{2\pi}{3}$). The field profile of this phased array dipoles should match the field profile of the mode with that negative group velocity. On the other hand, the mode with a positive group velocity obtains a phase lead of $\frac{2\pi}{3}$ as it propagates a_0, mismatching the phased array dipoles. Therefore, this source selectively excites the mode with a negative group velocity.

CHAPTER 3

UNFOLDING THE REFLECTION PATTERN

3.1 Start from the Dispersion Relation

The idea is to understand the interface as an electromagnetic boundary problem — a refraction from a waveguide to the free space. We only need to know the dispersion relations of the waveguide and the free space and a interface condition joining them. According to figure 2.5 (c), the Topologically Protected Kink Modes (TPKMs) are at dimensionless frequency $\frac{\omega a}{2\pi c} = 0.445$ with a momentum of $k_{kink}a_0 = \frac{4\pi}{3}$. The other side, vaccum, has the dispersion relation of isotropic free space. In addition, at the interface between the PTI and vacuum, the parallel component of the wave vector $k_{\|}$ is continuous, or, changed by N additional wave vectors, due to the periodicity of the photonic crystal.

$$k_{\|}a_0 = k_{kink}\, cos(60^\circ) = \frac{2\pi}{3} \tag{3.1}$$

or

$$k_{\|}a_0 = k_{kink}\, cos(60^\circ) \pm Nk' = \frac{2\pi}{3} \pm 2\pi N \tag{3.2}$$

Therefore, we can determine $k_{\|}$. With the dispersion relation in vacuum, we can also calculate $k_{\perp}$ and the angle of the refracted light in the following way.

$$k_{\|}^2 + k_{\perp}^2 = \varepsilon(\frac{\omega}{c})^2 \tag{3.3}$$

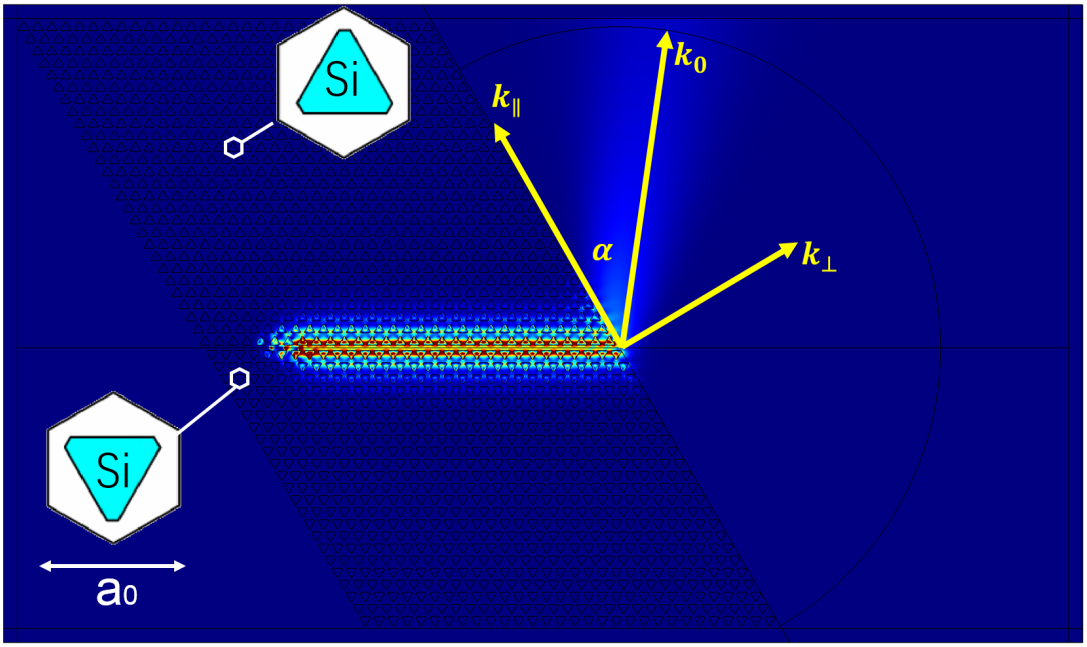

Figure 3.1: Refraction of TPKM from PTI into air

and

$$\alpha = arctan(\frac{k_{\parallel}}{k_{\perp}}) \tag{3.4}$$

This calculation provides accurate estimation of the direction of the refracted light. For example, when the free space is vacuum ($\varepsilon = 1$), only the $N = 0$ case provides a real $k_{\perp}$. This calculation gives $\alpha = 41.49°$. (figure 3.1) Compared to angular distribution of the energy of the refracted beam (figure 3.2 (c)), this result correctly indicates, along which direction, the energy is maximized.

3.2 A Model Based on Discrete Dipoles

As we are trying to investigate the refraction pattern further, the periodic nature of the photonic crystal suggests us to model it with an array of discrete electric

(and magnetic) dipoles. In addition, in this study, we focus on the TE-polarized (i.e. E field in plane and H field perpendicular to plane) mode. Therefore, we extract the electric field profile of the unit cells and try to model them as electric dipoles.

$$\vec{p} = \iint_{Si} i\omega(\varepsilon_{Si} - \varepsilon_{air})\varepsilon_0 \vec{E} \tag{3.5}$$

Since the system is 2-dimensional, the integration is over a surface instead of a volume. The subscript "Si" means that the integration is over the silicon region in a unit cell. ε_0 is the vacuum permittivity.

To come up with a simple and intuitive model from this discretization method, we need to reconstruct the refraction pattern, with as less unit cells as we can. (If we model all the unit cells with dipoles, these dipoles will reconstruct the field everywhere, but then the model will not be simple.) Therefore, we consider only the unit cells that are at the boundary of the PTI. According to the field profile given by the driven simulation, those unit cells that are spatially-further from the kink mode have lower field intensity. We can neglect them without introducing much numerical error. Therefore, we extract the field profiles of the 12 unit cells that are at the boundary and most close to the kink mode. Then, we study the overall radiation of the 12-dipole system.

By comparing the angular distribution of the emitted energy, we found that the 12-dipole system almost reconstructs the refraction pattern of the PTI. Therefore, we proceed to scrutinize these twelve dipoles. The first notable property of the twelve dipoles is that all of them are almost linarly polarized. Although all of them are actually elliptically polarized, their polarization ellipses have major

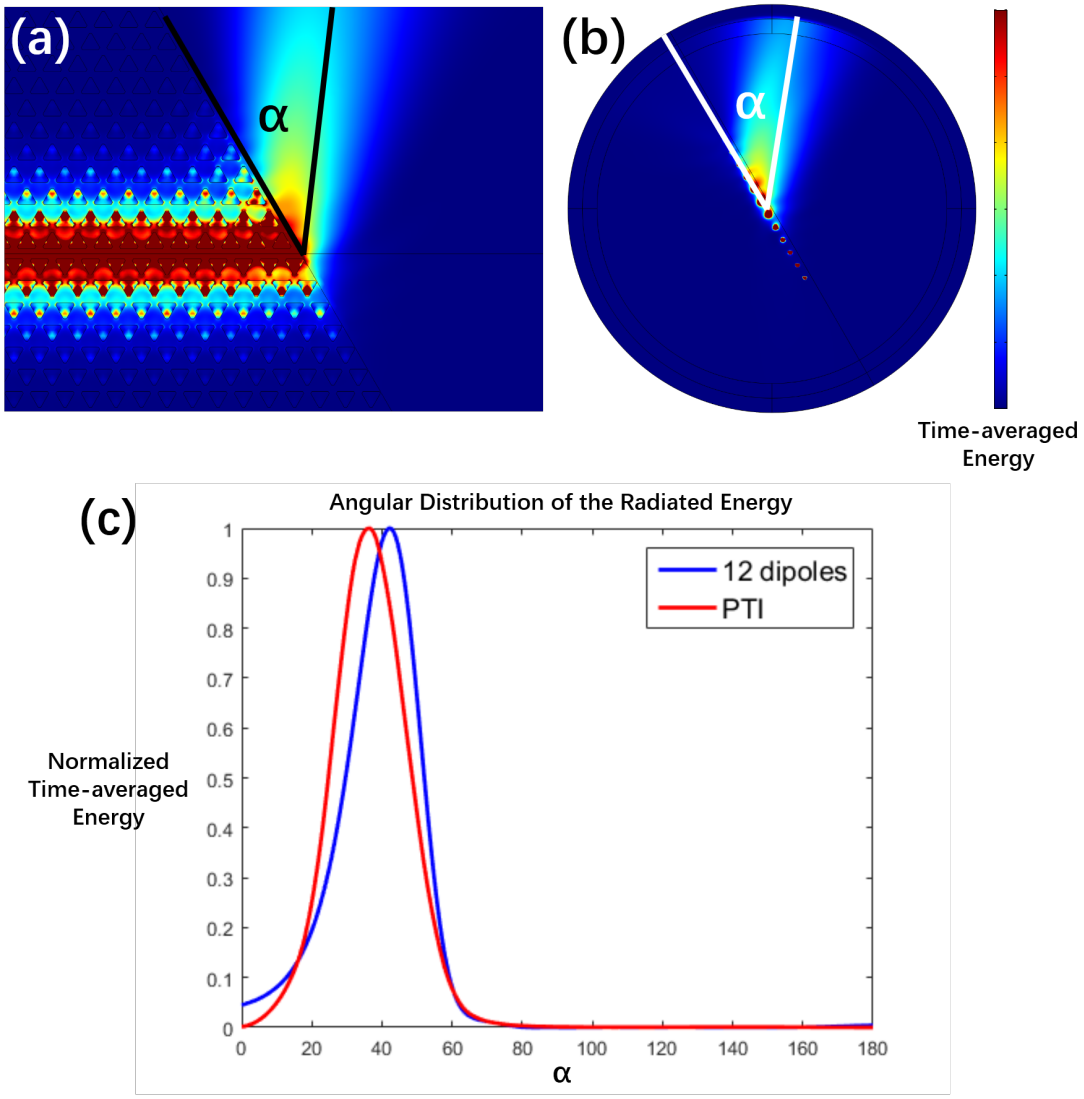

Figure 3.2: Comparison between the PTI and the 12-dipole system

axes that are much longer than the minor axes.

This linearly-polarized property of the twelve dipoles is peculiar. Because, a linearly polarized dipole is supposed to radiate a ”doughnut-like” pattern in 3D space — zero energy along the direction parallel to the dipole and maximum energy along the direction perpendicular to the dipole[11]. On a 2D plane

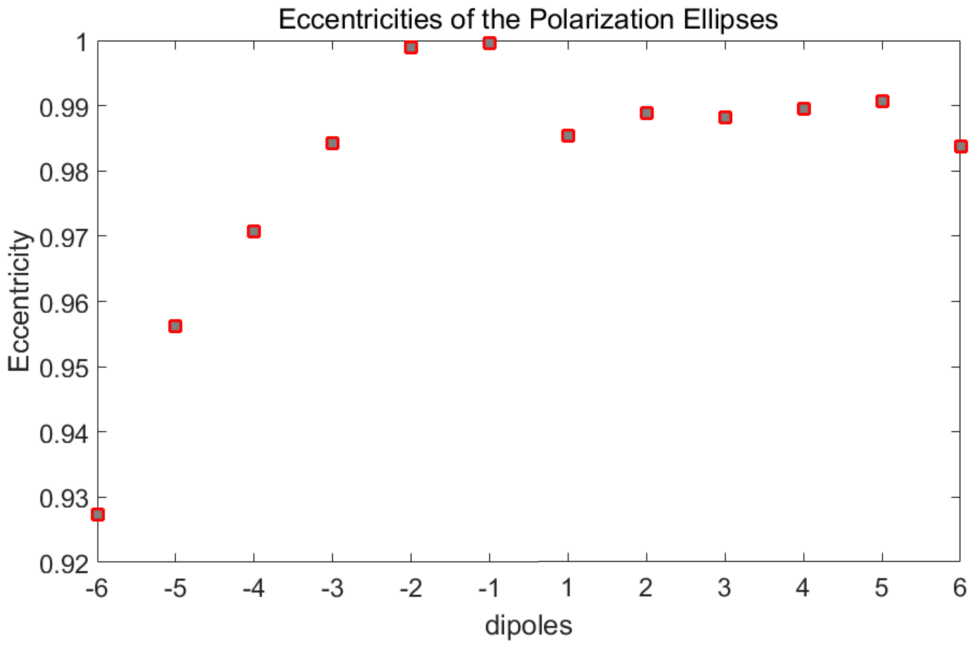

Figure 3.3: Eccentricities of the Polarization Ellipses

For all the elliptically polarized dipoles, the eccentricities are very close to one. Therefore the ellipses are very "flat". The dipoles are very close to linearly polarized.

cutting that doughnut vertically, the radiation pattern becomes a "dumbell" pattern. (Figure 3.2) However, the 12-dipole system is radiating along one direction, without the backward radiation.

Then, we start to suspect that, it may be the slightly-elliptical polarization that makes the difference, preventing them from radiating as completely-linearly polarized dipoles do. Therefore, we calculate the direction of the major axis of each of the twelve dipoles, calculate the average and choose that as the average-direction of the 12-dipole system. Then, we project every dipole along that average-direction and construct a new 12-linearly-polarized-dipole system.

However, by comparing the radiation pattern of the two systems, we find

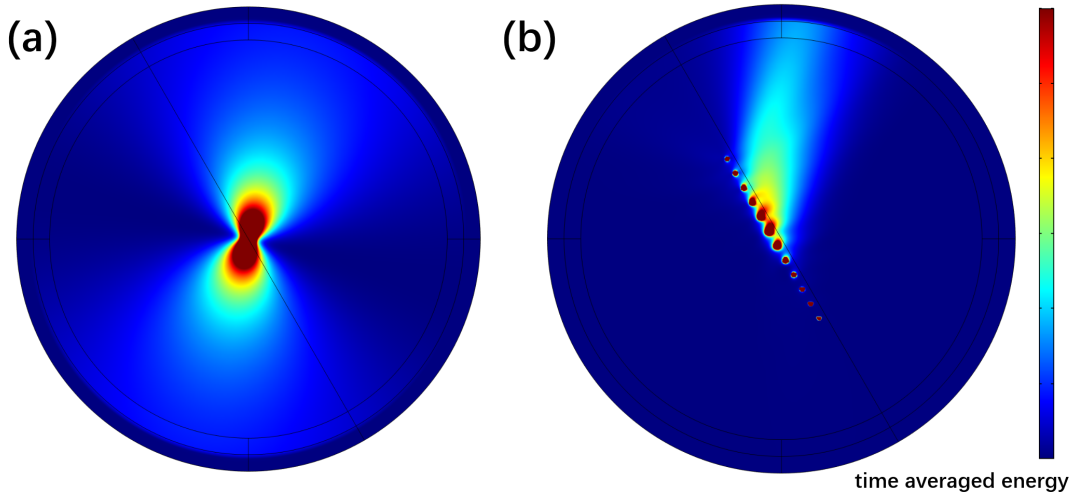

Figure 3.4: The radiation patterns of one dipole and the 12-dipole system

that they are very similar. Hence, we conclude that the peculiar radiation from the 12-dipole system is not due to their elliptical polarization.

While analyzing the polarization of the twelve dipoles, we notice the second unique feature of them. Every two adjacent dipoles have a phase difference close to $\frac{2\pi}{3}$. To understand this specific number of phase difference, we can consider the wavevector along the PTI/vacuum interface. At the interface, $k_{\|} = \frac{2\pi}{3}$, and the separation between two adjacent unit cell is the lattice constant $a_0 = 1$. Hence, every two dipoles extracted from two adjacent unit cells share the phase difference of $\frac{2\pi}{3}$. To investigate how this specific phase-difference affect the radiation pattern of the 12-dipole system, we set another twelve dipoles and manually divide their dipole moments correspondingly by $e^{\frac{2\pi}{3}}$, $e^{\frac{4\pi}{3}}$, $e^{\frac{6\pi}{3}}$, etc. This procedure removes from the dipoles the phase-difference caused by the spatial distances between them.

The radiation pattern in figure 3.5 (a) shows that, without that phase dif-

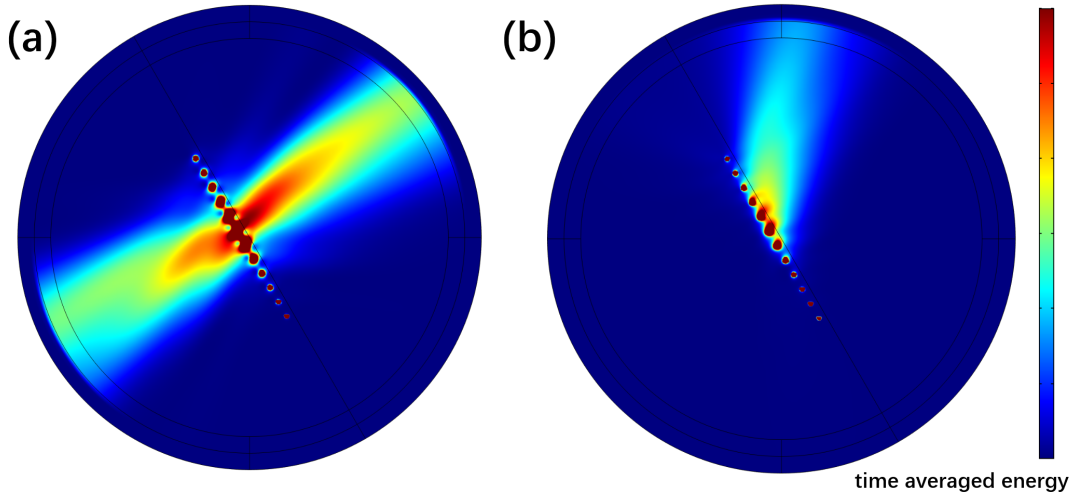

Figure 3.5: The radiation patterns of 12 phased and unphased dipoles

(a) The radiation pattern of the 12 dipoles after artificially phase-matching. (b) The radiation pattern of the original 12 dipoles extracted from the driven simulation

ference of $\frac{2\pi}{3}$ between every adjacent two dipoles, the twelve dipoles radiate in a similar way as linearly-polarized dipoles do — the most radiated energy is concentrated along the two opposite directions perpendicular to the dipoles' oscillation direction. Very different from figure 3.5 (a), figure 3.5 (b) shows that the 12-dipole system that reconstructs the PTI's refraction pattern radiates only along one direction. Therefore, we conclude that the phase difference between every two adjacent unit cells causes the peculiar radiation pattern.

3.3 How things get complex

At the beginning of this chapter, we estimate the angle of refraction into air according to the dispersion relations. Further, we model the refraction from PTI

into free-space with the radiation of a 12-dipole system. We discover that the phase-differences between every two adjacent dipoles lead to the unique redia-tion of the 12-dipole system. Therefore, these calculations unfold the refraction phenomenon, at least, at a preliminary level. However, equation 3.2 suggests a possibility of seeing multiple refraction lobes. If we fill the free space with a dielectric material with a enough high permittivity value, it is possible for the $k_{\|}$ altered by $N\frac{2\pi}{a_0}$ to form another refraction lobe. In the next chapter, we are going to first demonstrate that secondary lobe exists, then investigate which parame-ters affect the direction of that lobe, and finally tune these parameters to let the two lobes to be along the angles that we desire.

CHAPTER 4

ENGINEERING THE PHOTONIC BAND DIAGRAM

4.1 Filling the vacuum

To let two refraction lobes to exist, equation 3.2 and equation 3.3 should provide a real $k_\perp$. In the following paragraphs, we call the refraction lobe associated with 3.1 the 0th order lobe. That zero says that the $k_\parallel$ does not have any additional $\frac{2\pi}{a_0}$. Correspondingly, we call the refraction lobe associated with $N = 1$ in equation 3.2 the 1st order lobe. When the free space is air ($\varepsilon = 1$), the 1st order lobe has a $k_\perp = 0.4964i$, and therefore, it does not propagate into the free space. Letting $k_\perp = 0$, we can solve the minimum permittivity value of the dielectric filling the free space to let the 1st order to exist. That ε_{min} is 2.25.

With both 0th and 1st order lobes existing, we can use equations 3.1, 3.2, 3.3 and 3.4 to estimate the angles of both the two lobes accurately. For example, when the $\varepsilon_{freespace} = 2.8040$, the two peaks in the angular distribution of the energy refracted from PTI agrees with the calculation. (figure 4.1)

We return to our 12-dipole model, for this case of two refraction lobes. Comparing the angular dependence of the radiation patterns, we find that the 12-dipole still reconstructs the refraction. (figure 4.2 (c))

Figure 4.2 (c) shows a very intriguing feature — the angle between the two lobes is close to 90°. It is not possible for an array of parallel linearly-polarized dipoles in an isotropic medium to radiate along two perpendicular directions in the far field, because, with one direction perpendicular to the dipoles' oscillation, the other direction must be parallel to the oscillation. The far-field

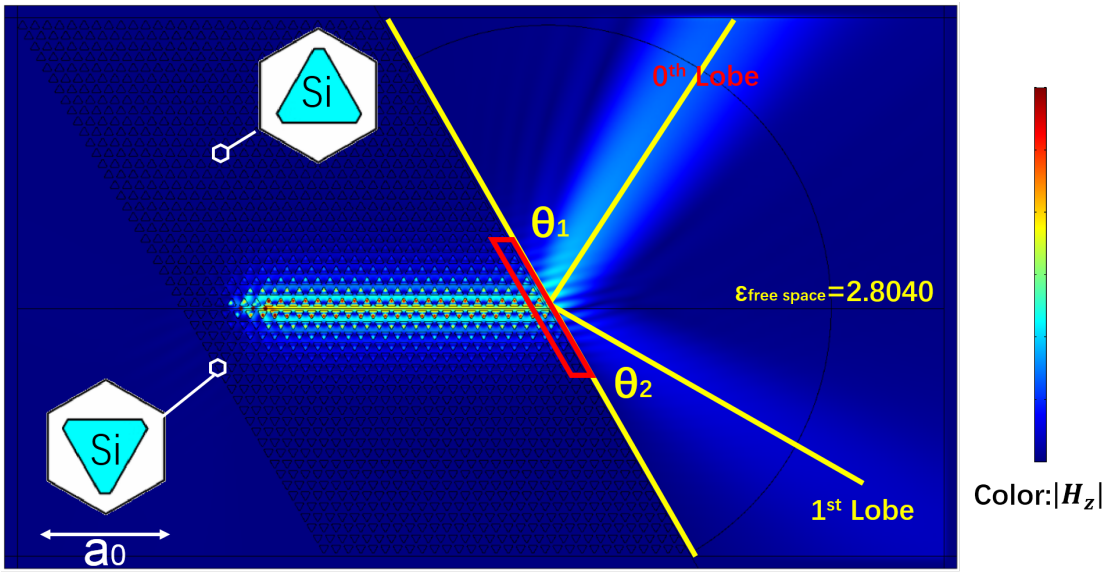

Figure 4.1: Field Profile When the Free Space is Filled with Dielectric ε = 2.8040

radiation along the dipoles' oscillation direction must be zero. This scenario is similar to a discretized Brewster's angle effect described in [25].

However, in figure 4.2 (c), the right and the left parts of the domain have different permittivitys. The medium is no longer isotropic, so this phenomenon can be understood as a refraction happening at the interface. The 1st order lobe is not parallel to the oscillation direction of the dipoles.

Therefore, we try to find an alternative way to search for a refraction pattern that is similar to the discretized Brewster's angle effect. We restore the permittivity of the free space to one. Equations 3.1, 3.2, 3.3 and 3.4 suggest that, at a higher dimensionless frequency $\frac{\omega a_0}{2\pi c}$, the refraction pattern into air ($\varepsilon = 1$) will contain two perpendicular directional lobes.

However, that 90° angle in $\varepsilon = 1$ medium requires $\frac{\omega a_0}{2\pi c} = 0.61$. This number

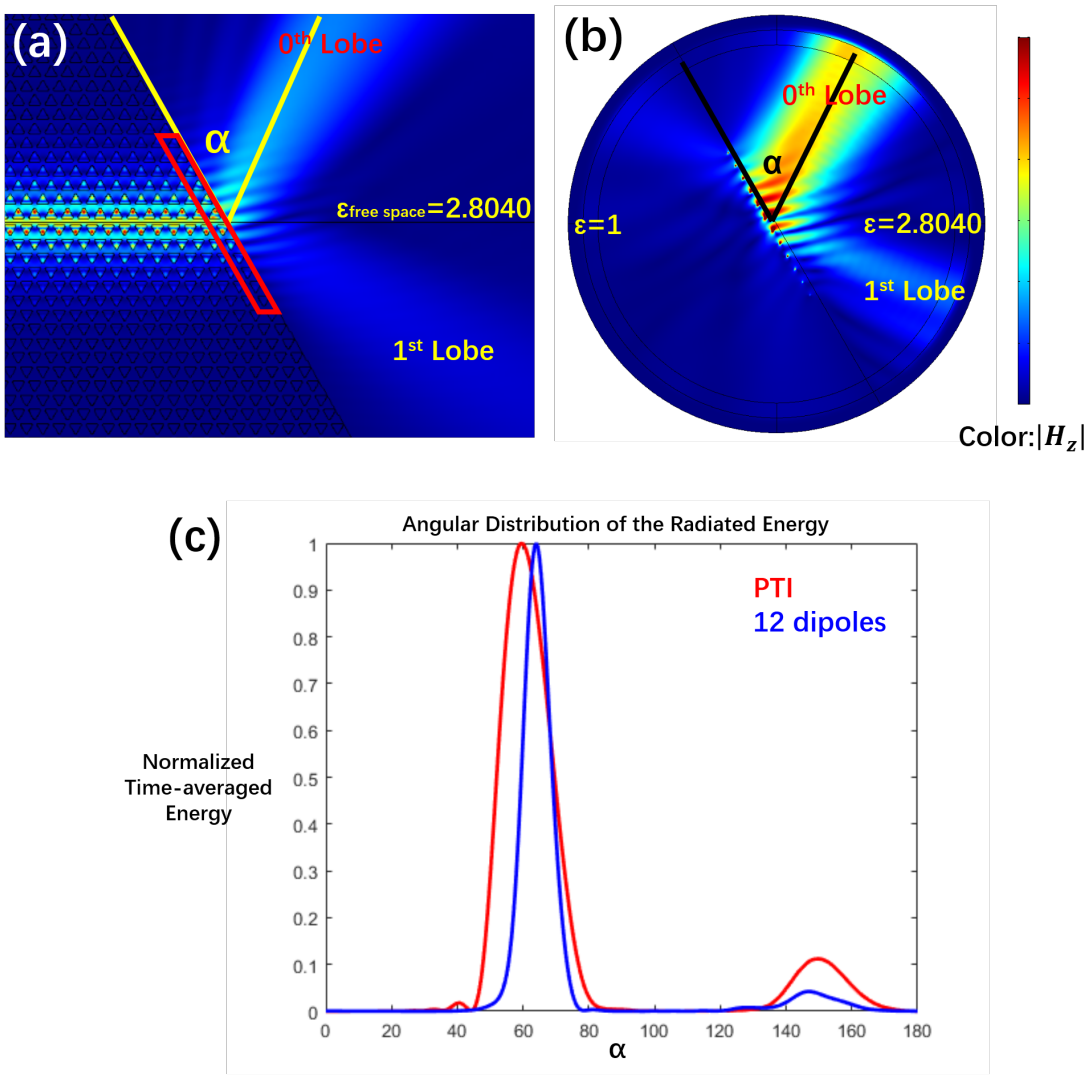

Figure 4.2: Comparison between the PTI and the 12-dipole System When the Free Space is Filled with Dielectric ε = 2.8040

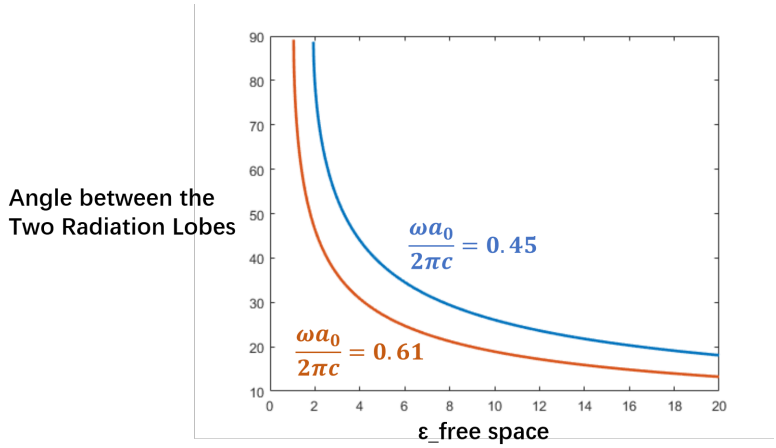

Figure 4.3: Angle between the Two Directional Lobes

exceeds the dispersion relation of the TPKM. (figure 2.5) Therefore, we try to taylor the dispersion of the TPKM by engineering the photonic crystal.

4.2 Carving the unit cell

The opening of the Dirac point at K(K′) point on the photonic band diagram (figure 2.4) is due to the inversion-symmetry-breaking geometric distribution of the permittivity over the unit cell. Therefore, the contrast between ε_{Si} and ε_{air} determines the scale of that inversion-symmetry-breaking. We can adjust that scale by replacing silicon with another dielectric material.

By changing the permittivity of the triangular-shaped rods, we discover that, a smaller scale of inversion-symmetry-breaking (i.e. a smaller permittivity) pushes the band gap to a higher dimensionless frequency $\frac{\omega a_0}{2\pi c}$ and vice versa. When the permittivity is too low, the band gap closes, preventing all topologically-nontrivial phenomena to happen.

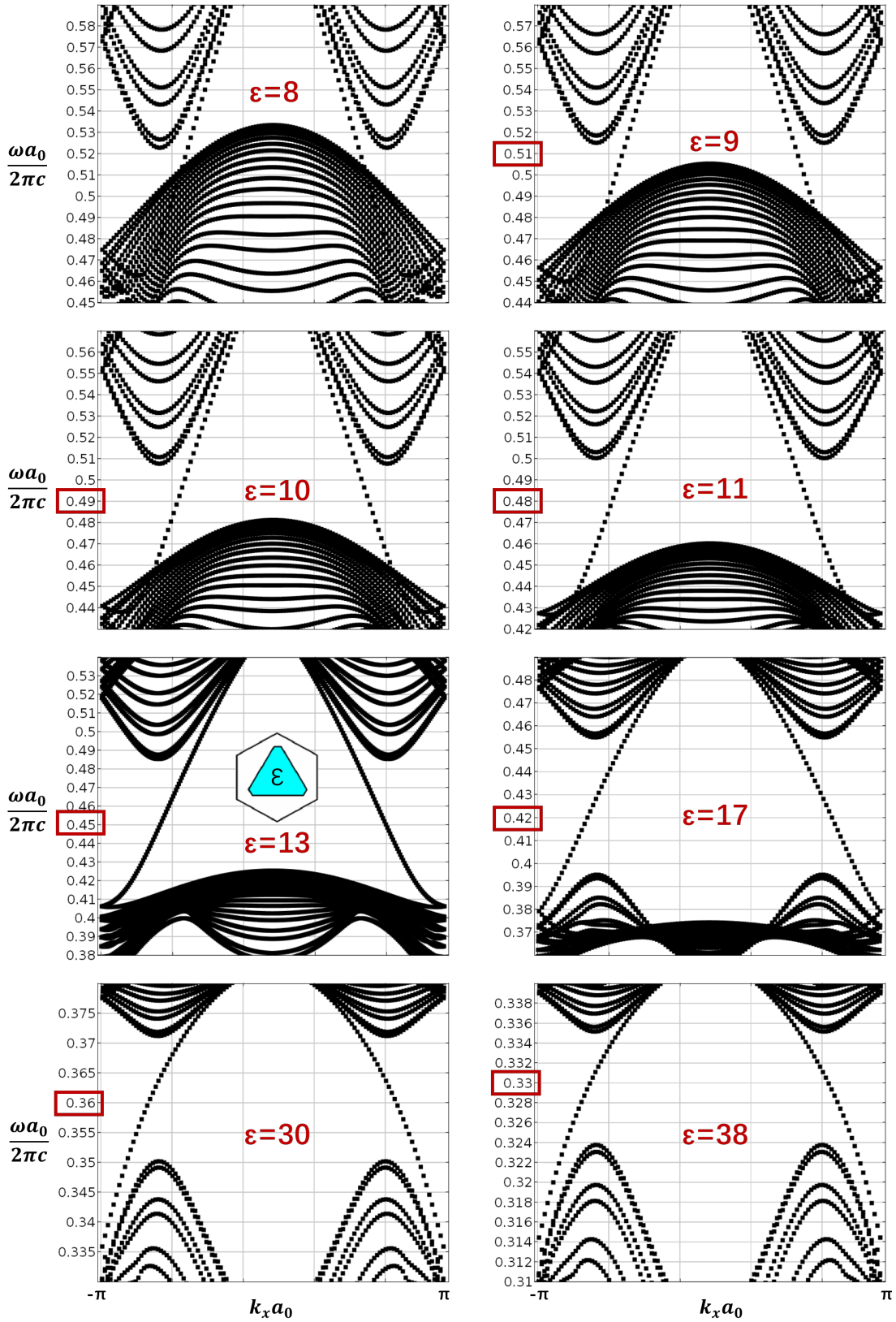

Figure 4.4: Modifying the band diagram

We also studied how the geometry affects the photonic band diagram. However, it is hard to quantify which geometry corresponds to a higher or lower scale of inversion-symmetry-breaking. We just present an example of a modified geometry and its photonic band diagram.

Meanwhile, we start to consider a "inversed" structure: in one unit cell, the silicon region and the air region are exchanged. The device is like a slab of silicon with a 2D-array of holes. Its photonic band structure was studied by Yaroslav A. Urzhumov and Gennady Shvets.[31] The advantage of this design is that, at the K(K') point, there are multiple degenerate points. One of them is at $\frac{\omega a_0}{2\pi c} = 0.62$ which may be related to a phenomenon similar to the Brewster's angle effect. After breaking the inversion symmetry, those degenerate points are opened as band gaps. However, those band gaps are different in principle. For the lowest-energy band gap, a TPKM may exist, while, for the high-energy band gap, no such TPKM exists. We further investigate this phenomenon by studying the topology.

4.3 Identifying topology — calculating the Chern number

The quantum valley Hall effect is due to inversion symmetry breaking in real space. The TPKM originates from a non-zero valley Chern number.

The eigen-frequency simulations of COMSOL provides numerical solutions to the photonic band diagram and the electromagnetic field distribution. The two solutions, analogous to the electronic band diagram and wave function in condensed matter electronic systems, determine the Chern number of the band diagram. We follow a numerical recipe[2, 7] to compute the Berry curvature

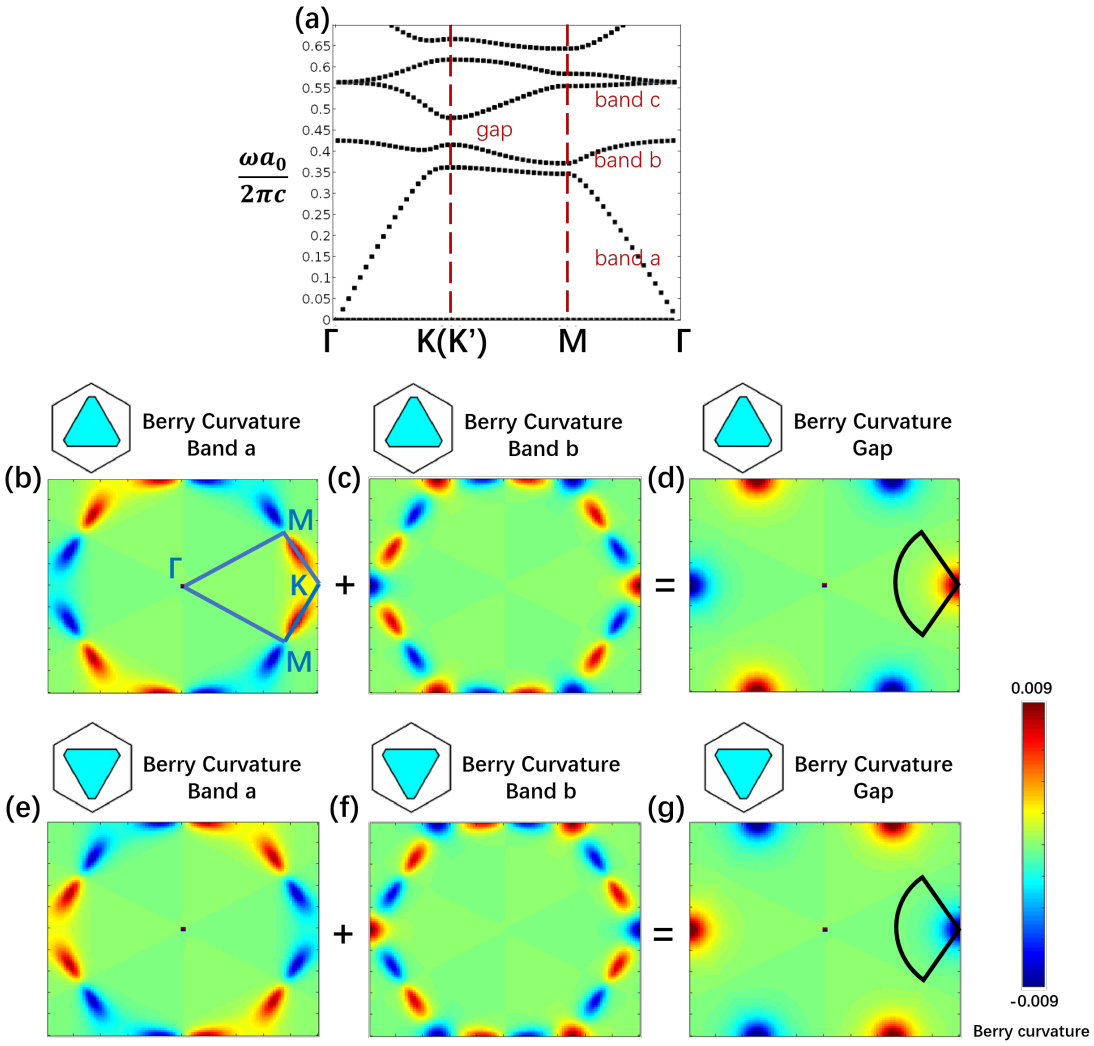

Figure 4.5: Berry Curvatures of the Two Differently Perturbed Unit Cells

over the first Brillouin zone and therefore calculate the Chern number.

For the original structure, triangular Si rods in air, the Berry curvatures of the two differently perturbed unit cells are shown in figure 4.5 (b), (c), (d), (e), (f) and (g). We are interested in the valley Chern number. We compute the K-valley Chern numbers associated with that complete band gap which is due to inversion-symmetry-breaking.

Both of the two bands below the band gap contribute to that gap valley Chern number. We sum the Berry curvatures of band a and band b and therefore obtain the Berry curvature associated with that band gap. We integrate that gap Berry curvature over the sector region close to the K point in figure 4.5 (c). According to the symmetry, this integration contributes $\frac{1}{3}$ of the gap valley Chern number assigned to the K-valley. We perform this calculation to the two different inversion-symmetry-broken unit cells and compute their difference. This difference indicates how many TPKM the interface can support. The result is expected to be,

$$\mathcal{N}_{gap,+,K} = \frac{1}{2\pi} 3 \iint_{sector} \Omega(\mathbf{k}) ds = \frac{1}{2} \tag{4.1}$$

and

$$\mathcal{N}_{gap,-,K} = \frac{1}{2\pi} 3 \iint_{sector} \Omega(\mathbf{k}) ds = -\frac{1}{2} \tag{4.2}$$

The subscript "+" (or "-") represents one type of inversion-symmetry-breaking, the triangular rod facing upwards (or downwards); "K" means that the Berry curvature is associated with the K-valley. Therefore, the number of supported TPKM that is polarized at the K-valley is,

$$\mathcal{N}_{gap,K} = \mathcal{N}_{gap,+,K} - \mathcal{N}_{gap,-,K} = 1 \tag{4.3}$$

For K'-valleys, the difference between the valley Chern numbers should also be 1. $\mathcal{N}_{gap,K'} = 1$

According to our computation, $\mathcal{N}_{gap,+,K} = 0.4263$ and $\mathcal{N}_{gap,-,K} = -0.4266$. Therefore, $\mathcal{N}_{gap,K} = 0.8529$. The nearest integer to this result is one, matching the fact that there is only one TPKM along the boundary. (figure 2.5).

The error is about 15%. A possible source of this error is the finite mesh of the momentum space for the calculation of the Berry curvature. We mesh the rectangular reciprocal space that contains the first Brillouin zone into $101^2 = 10201$ elements. This mesh gives $\Delta k_x = \frac{2\pi}{75}$ and $\Delta k_y = \frac{\sqrt{3}\pi}{75}$.

A possible source of the error is a numerical overflow that occurs at the Γ point of band a. We think that is due to a degeneracy of band a and a lower flat band. It is possible to separate the two bands by linear transformations and eliminate that numerical overflow.[7, 2] We are still improving our code and trying to use that technique to study the Berry curvature at degeneracy points. At present, we do not know how that degeneracy affects our calculation of the gap Chern number. In this study, we assume that the degeneracy at the Γ point casts negligible effect on the Berry curvature close to the K(K′) points, due to the large distance between Γ and K(K′) points in the reciprocal space.

For the ”inversed” unit cell, an air-hole in a silicon slab, a degeneracy point exists at $\frac{\omega a_0}{2\pi c} = 0.62$ close to the frequency for two perpendicular radiation lobes to occur. After inversion-symmetry-breaking, it becomes a complete band gap. Therefore, we are interested in the topology of this band gap. (band gap in figure 4.6 (a))

After summing the Berry curvatures of all the bands below, we obtain the Berry curvature of band gap (figure 4.6 (c)). However, the valley Chern number associated with band gap is 0.0851 from our calculation. This number is close to

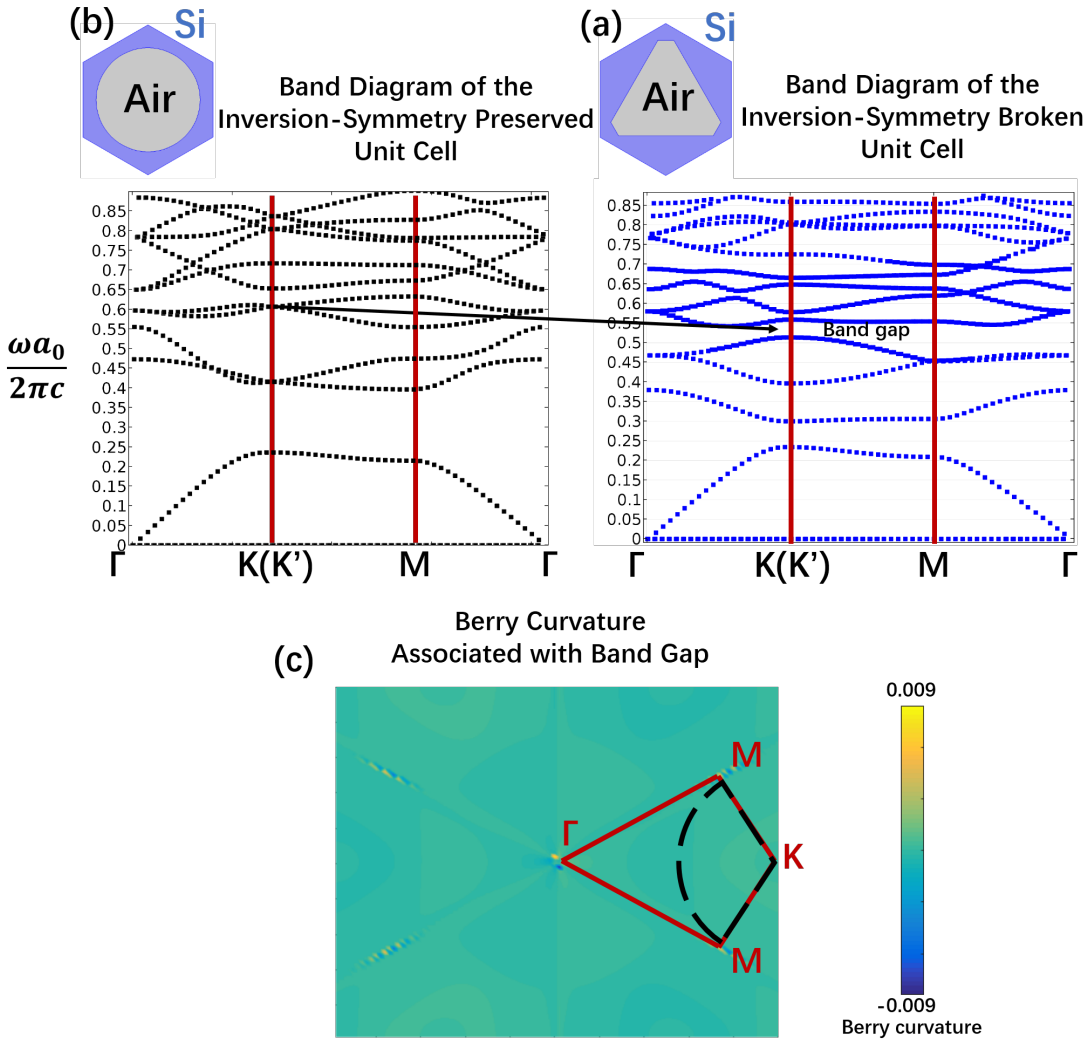

Figure 4.6: Berry Curvatures of the "Inversed" Unit Cells

0, indicating that no TPKM exists at the interface.

To confirm this discovery, we set up a supercell to simulate the kink mode at the boundary. The dispersion relation of that kink mode does not connect the bulk modes above and below the band gap. (figure 4.7) Therefore, that kink mode is topologically trivial. In this band gap, there is no TPKM, matching the zero result of the calculated gap valley-Chern-number difference.

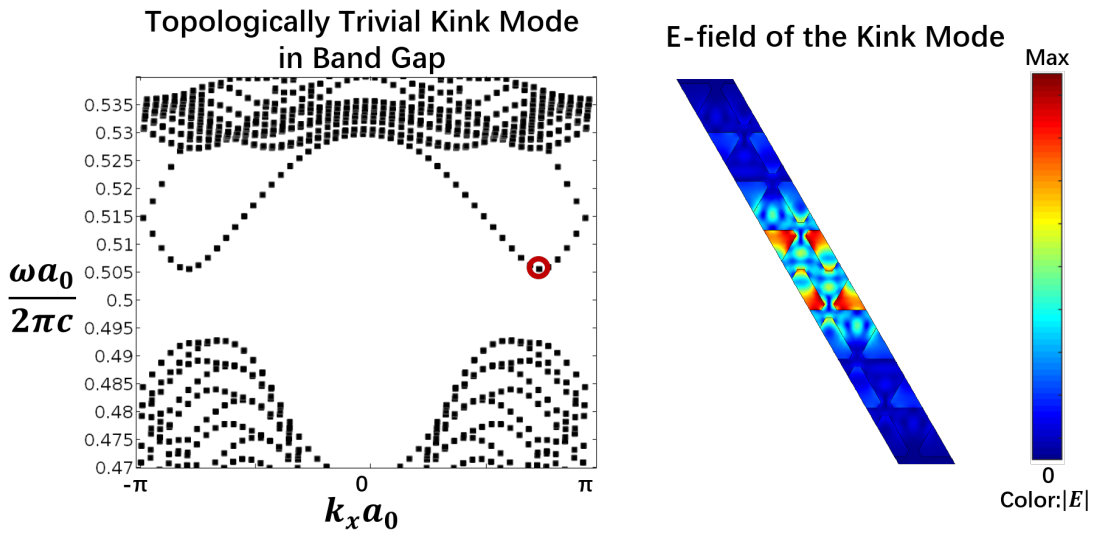

Figure 4.7: Topologically trivial kink mode in band gap

The E-field distribution is taken at $k_x a_0 = 2.6$ and $\frac{\omega a_0}{2\pi c} = 0.505$.

CHAPTER 5

FUTURE

5.1 Inverse Design — a General Solution?

We have tried to increase the frequency of the TPKM. However, our attempts do not cover all possible geometries in the C6v symmetric group. In fact, researchers have been using optimization algorithms to design photonic structures. [18, 30, 17] The method is called "inverse design" and, thoeretically, it can sweep over all possible geometric alignments within a particular symmetric group, for example, in 2D, the C4v or the C6v group. With this method, we can ultimately find out how high we can push the TPKM to. If a TPKM can exist at $\frac{\omega a_0}{2\pi c} = 0.61$, the discrete Brewster's angle effect could exist.

5.2 Proceed to Applications

Till now, most experimentally realize PTIs in microwave spectrum. [29, 22, 33] In this spectrum, not only can we apply high magnetic field, but also the source can be enclosed inside the PTI to excite the TPKM. However, in nano-fabricated optical devices, it is extremely hard to include the source. Using inverse design, we may create a sophisticated pattern which can couple the radiation from the 12-dipole system to a horizontal wave. Therefore, by attaching that pattern to the edge of the 2D Si PTI, we can excite the twelve unit cells at the boundary with a horizontal wave. Then, according to reciprocity, those twelve unit cells will excite the TPKM in the PTI.

5.3 Convergence of the Chern Number Computation

We calculated the valley Chern number of the band gap. Our numerical result is 15% apart from one. We assume that the error is due to the finite size of the mesh elements in the reciprocal space. With the discrete nature of the numerical recipe[7], such error always exists. In this study, the supercell simulation (figure 2.5) showing one TPKM, supports our numerical calculation of the Chern number. But, how to justify the accuracy (or the effectiveness) of the numerical calculation? We expect that the error will reduce as we increase the number of mesh elements of the reciprocal lattice. By repeating the calculation with decreasing size of mesh elements, we may demonstrate that the numerical result should converge to a quantized Chern number.

BIBLIOGRAPHY

[1] Comsol multiphysics reference manual, version 5.3, 2017.

[2] János K. Asbóth, László Oroszlány, and András Pályi. *A Short Course on Topological Insulators*. Springer International Publishing, Springer, 1 edition, 2016.

[3] Neil W. Ashcroft and N. David Mermin. *Solid State Physics*. Saunders College, Philadelphia, 1976.

[4] Michael Victor Berry. Quantal phase factors accompanying adiabatic changes. *Proceedings of the Royal Society of London. A. Mathematical and Physical Sciences*, 392:45–57, Nov 1984.

[5] Jian-Wen Dong, Xiao-Dong Chen, Hanyu Zhu, Yuan Wang, and Xiang Zhang. Valley photonic crystals for control of spin and topology. *Nature Materials*, 28:1–6, Nov 2016.

[6] Kejie Fang, Zongfu Yu, and Shanhui Fan. Realizing effective magnetic field for photons by controlling the phase of dynamic modulation. *Nature Photonics*, 6:782–787, Aug 2012.

[7] Takahiro Fukui, Yasuhiro Hatsugai, and Hiroshi Suzuki. Chern numbers in discretized brillouin zone: Efficient method of computing (spin) hall conductances. *Journal of the Physical Society of Japan*, 74:1674–1677, June 2005.

[8] S. Ali Hassani Gangaraj, Andrei Nemilentsau, and George W. Hanson. The effects of three-dimensional defects on one-way surface plasmon propagation for photonic topological insulators comprised of continuum media. *Scientific Reports*, 6:30055, July 2016.

[9] Fei Gao, Haoran Xue, Zhaoju Yang, Kueifu Lai, Yang Yu, Xiao Lin, Yidong Chong, Gennady Shvets, and Baile Zhang. Topologically protected refraction of robust kink states in valley photonic crystals. *Nature Physics*, 14:140–145, Nov 2017.

[10] Mohammad Hafezi, Eugene A. Demler, Mikhail D. Lukin, and Jacob M. Taylor. Robust optical delay lines with topological protection. *Nature Physics*, 7:907–912, Aug 2011.

[11] John David Jackson. *Classical Electrodynamics*. New York: John Wiley and Sons, Springer, 3 edition, 1999.

[12] John D. Joanopoulos, Steven G. Johnson, Joshua N. Winn, and Robert D. Meade. *Photonic Crystals: Molding the Flow of Light*. Princeton University Press, Princeton, 2008.

[13] Long Ju, Zhiwen Shi, Nityan Nair, Yinchuan Lv, Chenhao Jin, Jairo Velasco Jr, Claudia Ojeda Aristizabal, Hans A. Bechtel, Michael C. Martin, Alex Zettl, James Analytis, and Feng Wang. Topological valley transport at bilayer graphene domain walls. *Nature*, 520:650–655, April 2015.

[14] Jeil Jung, Fan Zhang, Zhenhua Qiao, and Allan H. MacDonald. Valley-hall kink and edge states in multilayer graphene. *Phys. Rev. B.*, 84, Aug 2011.

[15] Alexander B. Khanikaev, S. Hossein Mousavi, Wang-Kong Tse, Mehdi Kargarian, Allan H. MacDonald, and Gennady Shvets. Photonic topological insulators. *Nature Materials*, 12:233–239, Dec 2012.

[16] K. V. Klitzing, G. Dorda, and M. Pepper. New method for high-accuracy determination of the fine-structure constant based on quantized hall resistance. *Physical Review Letters*, 45, Aug 1980.

[17] Zin Lin, Adi Pick, Marko Lonăr, and Alejandro W. Rodriguez. Enhanced spontaneous emission at third-order dirac exceptional points in inverse-designed photonic crystals. *Phys. Rev. Lett.*, 117:107402, August 2016.

[18] Jesse Lu and Jelena Vučković. Nanophotonic computational design. *Optics Express*, 21:13351, May 2013.

[19] Ling Lu, John D. Joannopoulos, and Marin Soljačić. Topological photonic. *Nature Photonics*, 8, Sept 2014.

[20] Tzuhsuan Ma, Alexander B. Khanikaev, S. Hossein Mousavi, and Gennady Shvets. Topologically protected photonic transport in bi-anisotropic metawaveguides, 2014.

[21] Tzuhsuan Ma and Gennady Shvets. All-si valley-hall photonic topological insulator. *New Journal of Physics*, 18(2):025012, 2016.

[22] Tzuhsuan Ma and Gennady Shvets. Scattering-free edge states between heterogeneous photonic topological insulators. *Phys. Rev. B.*, 95, April 2017.

[23] Mikio Nakahara. *Geometry, Topology and Physics*. Taylor and Francis Group, London, 1990.

[24] Shivaramakrishnan Pancharatnam. Generalized theory of interference, and its applications. part i. coherent pencils. *Proceedings of the Indian Academy of Sciences, Section A*, 44:247–262, 1956.

[25] Ramón Paniagua-Domínguez, Ye Feng Yu, Andrey E. Miroshnichenko, Leonid A. Krivitsky, Yuan Hsing Fu, Vytautas Valuckas, Leonard Gonzaga, Yeow Teck Toh, Anthony Yew Seng Kay, Boris Lukyanchuk, and Arseniy I. Kuznetsov. Generalized brewster effect in dielectric metasurfaces. *Nature Communications*, 7:1–9, Jan 2016.

[26] Srinivas Raghu and Frederick Duncan Michael Haldane. Analogs of quantum-hall-effect edge states in photonic crystals. *Phys. Rev. A.*, 78:033834, Sept 2008.

[27] Srinivas Raghu and Frederick Duncan Michael Haldane. Possible realization of directional optical waveguides in photonic crystals with broken time-reversal symmetry. *Phys. Rev. Lett.*, 100:013904, Jan 2008.

[28] Concita Sibilia, Trevor M. Benson, Marian Marciniak, and Tomasz Szoplik. *Photonic Crystals: Physics and Technology*. Springer Science and Business Media, Berlin/Heidelberg Germany, 2009.

[29] Scott A. Skirlo, Ling Lu, Yuichi Igarashi, Qinghui Yan, John Joannopoulos, and Marin Soljačić. Experimental observation of large chern numbers in photonic crystals. *Physical Review Letters*, 115, Apr 2015.

[30] Logan Su, Rahul Trivedi, Neil V. Sapra, Alexander Y. Piggott, Dries Vercruysse, and Jelena Vučković. Fully-automated optimization of grating couplers. *Optics Express*, 26:4023, Feb. 2018.

[31] Yaroslav A. Urzhumov and Gennady Shvets. Extreme anisotropy of wave propagation in two-dimensional photonic crystals. *Phys. Rev. E.*, 72:026608, August 2005.

[32] Z. Wang, Y. Chong, J. D. Joannopoulos, and M. Soljačić. Reflection-free one-way edge modes in a gyromagnetic photonic crystal. *Physical Review Letters*, 100, Jan 2008.

[33] Z. Wang, Y. Chong, J. D. Joannopoulos, and M. Soljačić. Observation of

unidirectional backscattering-immune topological electromagnetic states. *Nature*, 461:772–775, Oct 2009.

[34] Di Xiao, Ming-Che Chang, and Qian Niu. Berry phase effects on electronic properties. *Review of Modern Physics*, 82, Jan 2010.

[35] Di Xiao, Wang Yao, and Qian Niu. Valley-contrasting physics in graphene: Magnetic moment and topological transport. *Physical Review Letters*, 99, Dec 2007.